To appear in *Philosophical Magazine*
Vol. 00, No. 00, Month 20XX, 1–27

Solute Drag on Perfect and Extended Dislocations

R.B. Sills[a,b*] and W. Cai[a]

[a]*Department of Mechanical Engineering, Stanford University, CA 94305, USA;*
[b]*Sandia National Laboratories, Livermore, CA 94551, USA*

(*Submitted October 2015*)

The drag force exerted on a moving dislocation by a field of mobile solutes is studied in the steady state. The drag force is numerically calculated as a function of the dislocation velocity for both perfect and extended dislocations. The sensitivity of the non-dimensionalized force-velocity curve to the various controlling parameters is assessed, and an approximate analytical force-velocity expression is given. A non-dimensional parameter S characterizing the strength of the solute-dislocation interaction, the background solute fraction χ_0, and the dislocation character angle θ, are found to have the strongest influence on the force-velocity curve. Within the model considered here, a perfect screw dislocation experiences no solute drag, but an extended screw dislocation experiences a non-zero drag force that is about 10% to 30% of the drag on an extended edge dislocation. The solutes can change the spacing between the Shockley partials in both stationary and moving extended dislocations, even when the stacking fault energy remains unaltered. Under certain conditions, the solutes destabilize an extended dislocation by either collapsing it into a perfect dislocation or causing the partials to separate unboundedly. It is proposed that the latter instability may lead to the formation of large faulted areas and deformation twins in low stacking fault energy materials containing solutes, consistent with experimental observations of copper and stainless steel containing hydrogen.

Keywords: dislocation, solute, drag, Cottrell atmosphere, extended dislocation

1. Introduction

Understanding drag forces induced by solute atoms on moving dislocations is a fundamental problem in materials science. Given the ubiquity of solid solutions and alloying in metallic systems, having a solid understanding of the interactions of point defects with dislocations is very important. These interactions are known to govern the behavior of metals during creep, yielding, and fatigue, and to give rise to a multitude of phenomena including yield drop, dynamic strain aging, and the Portevin-LeChatelier instability.

Cottrell and coauthors pioneered the study of solute-dislocation interactions in a series of works in the 1940s and 1950s. Cottrell [1] and Cottrell and Bilby [2] examined the equilibrium distribution of solutes surrounding a stationary edge dislocation, showing that the hydrostatic stress field beneath the dislocation half plane creates a region of elevated concentration as shown in Fig. 1(a); this concept is now commonly referred to as the Cottrell atmosphere. Cottrell and Jaswon [3] and Cottrell [4] studied the evolution of this atmosphere when the dislocation is in motion. Using a combination of analytical and numerical methods, it was shown that steady-state dislocation glide would distort the atmosphere and give rise to a drag force on the dislocation. Cottrell [4] then suggested that at some critical velocity, v_c, the drag force should exhibit a maximum.

Many authors have furthered our understanding of this problem. Yoshinaga and Morozumi [5]

*Corresponding author. Email: rbsills@stanford.edu

presented a numerical approach wherein they tracked the transient concentration field around a dislocation on a uniform grid. They simulated the transition of the atmosphere from the stationary to steady-state-moving distribution, and presented the first force-velocity curve, showing how the drag force per unit length of dislocation line, F, at steady-state was dependent on the velocity, v. (see Fig. 1(b) for a schematic depiction). Takeuchi and Argon [6] adopted this numerical approach as well, but focused on solving for the steady-state solution directly in the manner of Cottrell and Jaswon [3]. They presented force-velocity curves for pure glide, pure climb, and mixed glide-climb motion. All of these works focused only on the dilute limit of solid solutions, where the fact that only one solute atom can occupy each lattice site does not impact the results significantly. James and Barnett [7] were the first to extend the analysis to consider these site exclusion effects, in addition to the effects of a non-singular dislocation core using the Peierls-Nabarro model. Fuentes-Samaniego et al. [8] presented the analytical solution for the concentration field around a steadily moving singular dislocation in the dilute limit, and gave the analytical force-velocity curve in the limit of a slow dislocation. Finally, Zhang and Curtin [9] calculated the force-velocity curve for Al-Mg in a manner similar to Yoshinaga and Morozumi [5], using information from atomistic calculations to improve the accuracy of the calculation at the dislocation core. They found that the solutes at the core contributed an additional drag force at high velocities.

Despite the extensive literature on the subject of force-velocity curves, there is still disagreement concerning their basic features [10]. Even though all authors agree on the basic form of the force-velocity curve, as illustrated in Fig. 1, the shape of the curves differ and the critical velocity and maximum drag force vary by factors of 4 to 10 across the different approaches [8, 10]. Due to the complexity and nonlinearity of the partial differential equation governing the problem, a full analytical solution beyond the dilute limit is very challenging. Furthermore, calculating the force-velocity curve beyond the limit of slow dislocations analytically is also difficult [8]. The numerical studies on this problem, excluding Zhang and Curtin [9], were all conducted when computational capacity was very limited, making it difficult to ensure solutions were converged. Convergence is a real issue given the highly nonlinear and singular nature of a dislocation stress field, and the desire to study the problem in an infinite medium where boundary conditions are difficult to enforce.

With this work, we hope to address these limitations and advance the understanding of solute drag on dislocations. With modern computational tools, the accuracy of a numerical approach can be significantly improved relative to previous studies, and solution convergence can be readily verified. Furthermore, we will carry the analysis beyond the realm of perfect dislocations and consider the case of extended dislocations, where a dislocation has dissociated into two Shockley partials connected by a stacking fault. Since real dislocations in face-centered-cubic (FCC) and hexagonal close-packed (HCP) metals are extended, analyzing this case is important for understanding plasticity in these metals.

The remainder of this paper is organized as follows. First the relevant theoretical results will be briefly reviewed in Section 2. The methods used for computing both the concentration field and the drag force will be presented in Section 3. The results will be given in Section 4, first for perfect and then for extended dislocations. The significance and implications of the results will be discussed in Section 5. Conclusions will be presented in Section 6.

2. Theory

We are interested in determining the solute drag on a dislocation at steady state. To do so, we consider an infinitely long, straight dislocation positioned at the origin with its sense vector ξ along the $+z$-axis and its Burgers vector controlled by the character angle θ ($\theta = 0^\circ$ for screw with $\mathbf{b} = b\,\mathbf{e}_z$ and $\theta = 90^\circ$ for edge with $\mathbf{b} = b\,\mathbf{e}_x$) in an infinite, homogeneous, isotropic, linear elastic medium containing a population of mobile point defects (see Fig. 1(a)). These point defects can occupy

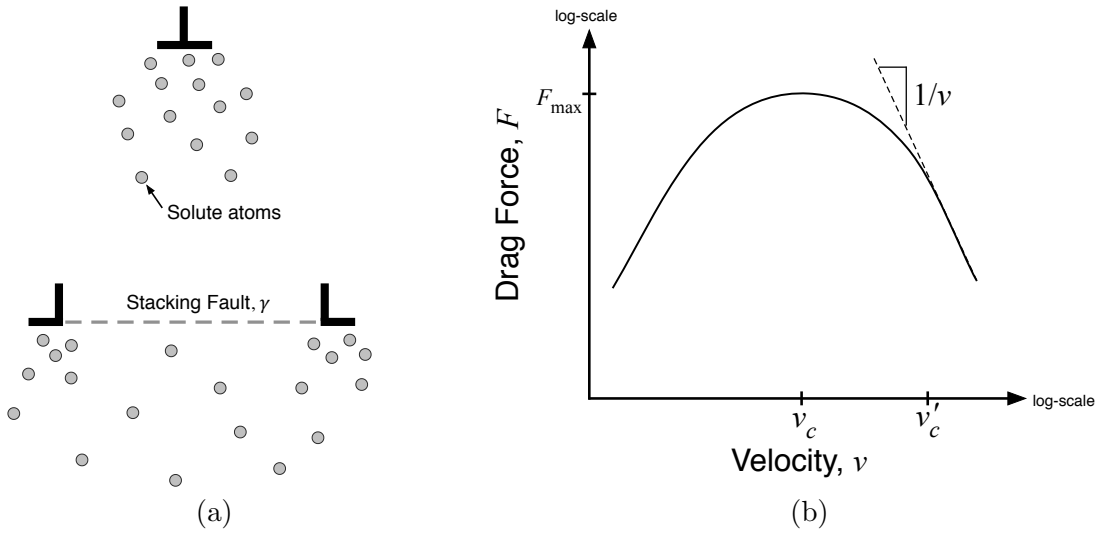

Figure 1. Schematic depictions of (a) Cottrell atmospheres around (top) perfect and (bottom) extended dislocations and (b) force-velocity curve with major features shown.

either interstitial sites or the main lattice sites as substitutional solutes, and their distribution is characterized by the concentration field $c(x, y)$. When inserted into the medium, these defects produce a spherically-symmetric distortion characterized by ΔV, the volume expansion due to each solute. In a real crystal not all solute atoms produce purely dilatational misfit fields, however, and in some systems deviatoric misfit effects can be important (e.g. carbon in iron). In these cases, additional parameters beyond those considered here may be necessary to quantify the misfit. In addition to a misfit, a modulus mismatch between the solute and matrix is known to lead to solute drag as well, and is especially important in the case of screw dislocations [11]. However, we assume here that the solute atoms can be treated as inclusions with the same elastic constants as the surrounding medium, and neglect modulus mismatch effects.

Given the spherically-symmetric nature of the defects, in this model solutes only interact with the hydrostatic stress field of the dislocation. The associated interaction energy is characterized by the potential $p_{\mathrm{d}}(x, y, b_{\mathrm{e}})\Delta V$, where $p_{\mathrm{d}}(x, y, b_{\mathrm{e}})$ is the pressure field of the dislocation and b_{e} is the edge component of the Burgers vector. The pressure field scales with the parameter

$$\beta \equiv \frac{\mu b_{\mathrm{e}}}{3\pi}\frac{1+\nu}{1-\nu}\Delta V \tag{1}$$

where μ is the shear modulus and ν is Poisson's ratio. In the case of an extended dislocation, the pressure field is the superposition of the field from each partial dislocation:

$$p_{\mathrm{d}}\left(x, y, b_{\mathrm{e}}\right) = p_{\mathrm{d}}\left(x - \frac{d}{2}, y, b_{\mathrm{e}}^{\mathrm{L}}\right) + p_{\mathrm{d}}\left(x + \frac{d}{2}, y, b_{\mathrm{e}}^{\mathrm{T}}\right) \tag{2}$$

where we have assumed the dislocation is centered on the origin, dissociated in the x-z plane with separation distance d, and $b_{\mathrm{e}}^{\mathrm{L}}$ and $b_{\mathrm{e}}^{\mathrm{T}}$ are the edge components of the Burgers vectors for the leading and trailing partials, respectively (see Fig. 2). Here we consider extended dislocations in FCC metals, with the edge components of the partial Burgers vectors related to the character angle

by

$$b_{\mathrm{e}}^{\mathrm{L}} = b_{\mathrm{p}} \sin\left(\theta - 30^{\circ}\right) \quad (3)$$

$$b_{\mathrm{e}}^{\mathrm{T}} = b_{\mathrm{p}} \sin\left(\theta + 30^{\circ}\right), \quad (4)$$

where $b_{\mathrm{p}} = b/\sqrt{3}$ is the magnitude of each partial Burgers vector.

Generally, p_{d} is a function of the dislocation velocity v through relativistic effects [10]. These effects are small, however, when v is much less than the speed of sound of the material, and we will neglect them. For numerical reasons to be discussed, in this work we utilize the non-singular theory of dislocations [12] to calculate the pressure field. In the non-singular theory, the Burgers vector is smeared out in space according to a distribution characterized by the core radius, a (see Appendix A). When $a \to 0$, the traditional singular pressure field is recovered. The value of the core radius (which is typically on the order of b) should be selected on the basis of more fundamental material models (atomistics, density functional theory, etc.). If an estimate for the core radius is unknown, calculations should be conducted over the expected range of radius values, with the variations incorporated as uncertainties. The pressure field of a non-singular dislocation is given in Appendix A.

The key reason for using the non-singular theory in this work is that it provides a self-consistent core treatment that is conducive to numerical methods (elaborated below). It is important to point out that core effects due to non-linear interatomic interactions at the dislocation core are not accounted for in this model; inclusion of these effects requires further input from atomistic models for specific material systems, for example using the approach of [13], [9], or [14]. In the studies of Zhang and Curtin, it was found that core effects most influenced the high velocity behavior (after the critical velocity), with little effect at lower velocities, so we expect our results in the high velocity regime to be most affected by our core treatment.

It is important to point out that the mechanism of solute drag presented here—that due to the formation of Cottrell atmospheres—is not necessarily relevant for all material systems and loading conditions. Cottrell drag only accounts for the drag forces exerted by solutes that are mobile enough to keep up with moving dislocations, which is most relevant at high temperatures or with small solute atoms, so that solutes can diffuse quickly.

In this work we will use the symbol χ to denote the solute fraction, $c/c_{\max}$, with c as the concentration in number of solutes per unit volume and $c_{\max}$ as the maximum concentration (all available lattice sites occupied). We can write $c_{\max} = z/\Omega$, where z is the number of sites per solvent atom and Ω is the volume per solvent atom; $z = 1$ for substitutional solutes and depends on the type of site occupied for interstitial solutes (e.g. $z = 1$ for octahedral sites in FCC metals). Note that with this definition, $0 \leq \chi \leq 1$. The background concentration in the solid is characterized by the parameter χ_0, the solute fraction in the absence of any hydrostatic stresses; without a dislocation, the entire solid would be at the solute fraction χ_0.

2.1. *Chemical potential and diffusion equation*

The chemical potential for the solutes, when enforcing site exclusion, is [7, 15–18]

$$\mu_{\mathrm{chem}} = E_{\mathrm{f}} + p_{\mathrm{d}} \Delta V + k_{\mathrm{B}} T \ln\left(\frac{\chi}{1-\chi}\right) \quad (5)$$

where E_{f} is the formation energy for each solute, k_{B} is Boltzmann's constant, and T is the absolute temperature. In this model, solutes only interact with each other through site exclusion effects, i.e. only one solute can occupy each site. We will frequently refer to the dilute limit, which we define as

the background concentration below which site exclusion effects are unimportant and solutes are non-interacting. In some material systems, solutes can interact in other ways not considered here (for example, H-H interactions in Ni [20]).

The diffusion equation for our system needs to consider diffusion in addition to drift (forcing) due to the motion of the dislocation. We wish to solve the problem in a coordinate system that moves with the dislocation. Assuming an isotropic diffusivity of D and that the dislocation moves only along the x-axis (glide only) at a constant velocity v, our diffusion equation is

$$\frac{\partial \chi}{\partial t} = -\frac{1}{c_{\max}} \left(\nabla \cdot \mathbf{J} \right) \tag{6}$$

where $\mathbf{J}$ is the flux vector given by[1]

$$\mathbf{J} = -\frac{D \chi c_{\max}}{k_{\mathrm{B}} T} \nabla \mu_{\mathrm{chem}} - \chi c_{\max} \mathbf{v}, \tag{7}$$

∇ is the gradient operator, and $\mathbf{v} = v\,\mathbf{e}_x$ is the velocity vector. The boundary condition in our infinite domain is $\chi\left(r \to \infty\right) = \chi_0$ where $r = \sqrt{x^2 + y^2}$. We seek a steady state solution such that $\frac{\partial \chi}{\partial t} = 0$, i.e.

$$0 = \nabla \cdot \mathbf{J}. \tag{8}$$

2.2. *Features of the force-velocity curve*

There are a number of analytical results that describe various features of the force-velocity curve. Here we will briefly summarize them so that we may make comparisons with our results. All of these results apply to a perfect dislocation.

2.2.1. Peak force

Estimates of the peak force and critical velocity at which it occurs have a broad spread in the literature. Cottrell and Jaswon [3] estimated that the peak force in the dilute limit is

$$F^{\max} \approx M \cdot \beta \chi_0 c_{\max}\,, \tag{9}$$

with $M = 17$. Cottrell [4] modified this estimate slightly to $M = 28$. The numerical studies of Takeuchi and Argon [6] and James and Barnett [7] found peak values about an order of magnitude lower, with the result in Takeuchi and Argon [6] being very sensitive to the finite difference grid size. James and Barnett [7] found that beyond the dilute limit the increase in peak force with concentration was sublinear (weaker than in the dilute limit, as discussed in the results section). Hirth and Lothe [10] estimated the peak force in the dilute limit when $\beta < k_{\mathrm{B}} T b$ to be

$$F^{\max} = \left(\frac{\beta}{k_{\mathrm{B}} T b} \right) \cdot \beta \chi_0 c_{\max}\,, \tag{10}$$

In Section 4.1 we will show that the peak force can vary significantly depending on the strength of the atmosphere (solute-dislocation interaction) and the background concentration, with the scaling

[1] In a substitutional solid solution, the diffusion coefficients of the solvent and solute species are generally different, and this leads to a diffusion flux that is different from that presented here [17]. For the sake of simplicity we neglect this effect and assume the diffusivities of all atomic species are equal, yielding Eq. (7).

predicted by Eq. (10) being correct when $\beta/(k_{\mathrm{B}}Tb)$ is small.

2.2.2. Critical velocity

Cottrell [4] estimated the critical velocity, where the drag force is maximized, to be

$$v_c = \frac{4Dk_{\mathrm{B}}T}{\beta}. \tag{11}$$

Numerical results in Takeuchi and Argon [6] and James and Barnett [7] show critical velocities about a factor of 4 lower. We will show in Section 4.1 that Cottrell's estimate is quite good as long as the background concentration is low (i.e. in the dilute limit).

2.2.3. High velocity limit

In the high velocity limit, e.g. $v \gg v_c$, Hirth and Lothe [10] have found an approximate relationship for the drag force. Above the threshold velocity

$$v_c' = \frac{D\beta}{k_{\mathrm{B}}Tb^2}, \tag{12}$$

the drag force is approximately given by

$$F \approx \frac{\pi\chi_0 c_{\max} D\beta^2}{k_{\mathrm{B}}Tb^2 v}. \tag{13}$$

Thus, in the high velocity limit, the drag force scales as $1/v$. Our results will demonstrate that this high velocity limit with $1/v$ scaling always exists, but the threshold velocity does not obey Eq. (12).

2.3. *Effects of extended dislocations*

The consideration of extended dislocations adds a number of new effects to the analysis. The Cottrell atmosphere contributes an additional force on each partial that can alter the separation distance between them, d. Furthermore, when solute atoms reside in the stacking fault they can alter the stacking fault energy, providing another mechanism for changing the separation distance. This effect is known as Suzuki segregation [10]. In this work we assume that the stacking fault energy is a constant that does not vary with the local solute concentration. Using our results, a first approximation for Suzuki effects can be made by simply adjusting the stacking fault energy based on the expected concentration in the stacking fault. As the dislocation begins moving, the solute atmosphere will change shape causing the forces due to the solutes to change, making d a function of dislocation velocity as well. It will be shown that the separation distance can change significantly during motion, in some cases going to zero or infinity (instability). Finally, we note that for perfect dislocations the character dependence of the atmosphere and force-velocity curve is rather simple (as shown in Section 4.1.2), because a change in character corresponds to a simple change in the edge component of the Burgers vector. In contrast, the relationship between the character angle and the partial Burgers vectors is more complicated. For instance, with a perfect screw dislocation no atmosphere is present since the stress state is pure shear, however an extended screw dislocation will have an atmosphere and nonzero drag force because both partials have edge components.

2.4. *Dimensional analysis*

In order to simplify the problem of solute drag while maintaining generality, we utilize dimensional analysis. Considering all of the physical parameters and variables that enter this problem for a perfect dislocation leads to the following list:

$$b,\ \mu,\ \nu,\ \chi_0,\ a,\ \Omega,\ \Delta V,\ c_{\max},\ k_{\mathrm{B}}T,\ D,\ \theta,\ v,\ F$$

According to the Buckingham Pi theorem, this list of 13 parameters comprising 3 dimensions (length, mass, time) yields a total of 10 non-dimensional groups. We choose the following set:

$$\overline{F},\ q,\ \chi_0,\ S,\ \theta,\ \frac{a}{b},\ \nu,\ c_{\max}\Omega,\ \frac{\Delta V}{\Omega},\ \frac{\Omega}{b^3}$$

where

$$q \equiv \frac{v\hat{\beta}}{4Dk_{\mathrm{B}}T}\,, \quad \overline{F} \equiv \frac{F}{\chi_0 c_{\max}\hat{\beta}}\,, \quad S \equiv \left(\frac{\hat{\beta}}{k_{\mathrm{B}}Tb}\right)^2\,,$$

and

$$\hat{\beta} \equiv \frac{\mu b}{3\pi}\frac{1+\nu}{1-\nu}\Delta V = \frac{\beta}{\sin\theta}.$$

We make use of the parameter $\hat{\beta}$ rather than β, because $\hat{\beta}$ is nonzero for a screw dislocation. Note that for an edge dislocation, $q = v/v_c$ according to Eq. (11). The parameter S controls the strength of the Cottrell atmosphere and is proportional to v_c'/v_c, the ratio of the high velocity threshold to the critical velocity. We have found that the non-dimensional groups ν, $c_{\max}\Omega$, $\Delta V/\Omega$, and Ω/b^3 do not have a significant effect on the force-velocity curve, and hence are excluded from the analysis.

For the problem of solute drag on an extended dislocation we must add the parameter $\hat{\gamma}$ (to be defined later), which is related to the stacking fault energy and applied stress ($\hat{\gamma} = \gamma$ at zero stress), necessitating the addition of one non-dimensional group. We choose the group $\hat{\gamma}/\mu b$.

This analysis leads to the non-dimensional expression

$$\overline{F} = \overline{F}\left(q, \chi_0, S, \theta, \frac{\hat{\gamma}}{\mu b}, \frac{a}{b}\right). \tag{14}$$

Detailing these functional dependencies is a key objective of this work. It will be shown that all of these groups exert an influence of the force-velocity curve in different ways. To make the notation clear, we have re-expressed all of the key results in Section 2.2 in terms of these non-dimensional groups in Table 1.

3. Methods

We will employ an approach very similar to that of James and Barnett [7], but with small differences in the numerical methods and a much finer computational grid.

Table 1. Literature expressions describing features of force-velocity curves in dimensional and non-dimensional forms.

Feature	Eq.	Dimensional	Non-dimensional	Non-dimen. Edge	Reference
Peak force	(9)	$F^{\max} = M\beta\chi_0 c_{\max}$	$\overline{F}^{\max} = M\sin\theta$	$\overline{F}_e^{\max} = M$	[3], [4]
Peak force, dilute, $S < 1$	(10)	$F^{\max} = \frac{\chi_0 c_{\max}\beta^2}{k_{\mathrm{B}}Tb}$	$\overline{F}^{\max} = \sqrt{S}\sin^2\theta$	$\overline{F}_e^{\max} = \sqrt{S}$	[10]
Critical velocity	(11)	$v_c = \frac{4Dk_{\mathrm{B}}T}{\beta}$	$q_c = 1/\sin\theta$	$q_{c,e} = 1$	[4]
High velocity threshold	(12)	$v_c' = \frac{D\beta}{k_{\mathrm{B}}Tb^2}$	$q_c' = S\sin\theta/4$	$q_{c,e}' = S/4$	[10]
High velocity force	(13)	$F = \frac{\pi\chi_0 c_{\max}D\beta^2}{k_{\mathrm{B}}Tb^2 v}$	$\overline{F} = \frac{\pi}{4}\left(\frac{S}{q}\right)\sin^2\theta$	$\overline{F}_e = (\pi/4)S/q$	[10]

3.1. *Solving for the concentration field*

We employ the finite difference method to discretize Eq. (8) on a series of grid points (x_i, y_j) and convert it into a system of algebraic equations in the solute fraction at each grid point, χ_{ij}. Because the pressure field of the dislocation varies dramatically near the core, a fine grid is required there. However, enforcement of the infinite boundary condition requires we solve the problem on a large domain. These two requirements thus make a simple uniform grid computationally intractable. Instead, we will employ coordinate transformations $X = g(x)$ and $Y = h(y)$ such that the problem is discretized uniformly in the transformed domain (X, Y), and spread out with high resolution near the dislocation core(s) in the physical domain (x, y); derivatives on the two domains can then be related using the chain rule [21]. We choose transformations similar to James and Barnett [7]:

$$g(x) = \frac{1}{\pi}\left[\tan^{-1}\left(\frac{1}{\alpha}\left(x - \frac{d}{2}\right)\right) + \tan^{-1}\left(\frac{1}{\alpha}\left(x + \frac{d}{2}\right)\right)\right] \tag{15}$$

$$h(y) = \frac{2}{\pi}\tan^{-1}\left(\frac{y}{\alpha}\right). \tag{16}$$

α is a scaling parameter that controls the grid in the physical domain. Note that while $h(y)$ clusters points near the origin, $g(x)$ clusters them near $x = d/2$ and $-d/2$; this feature allows for the grid to be fine near the cores of both partial dislocations in the case of an extended dislocation. With these transformations, we can discretize the transformed domain uniformly on a bi-unit square and apply conventional second order center-differenced finite difference expressions.

After discretizing Eq. (8), the result is a nonlinear system of algebraic equations in χ_{ij}. To solve this system, we employ the Newton-Raphson method. This method cannot converge if the pressure field of the dislocation is singular at the core. Hence, we instead use the non-singular dislocation theory.

3.2. *Drag force and separation distance calculation*

In order to calculate the drag force resulting from the concentration field, we must determine the sum of all the forces exerted by each line of solutes in the domain. For brevity, we have moved the details of the force calculation to Appendix A. The end result is that, after some analytical integration, a double integral must be evaluated on an infinite domain. To numerically evalute it, first we truncate the domain according to the chosen transformation function parameters. Then we perform the integration with the adaptive quadrature routine `quad2d` in MATLAB, using linear interpolation with the `griddedInterpolant` function to approximate the concentration values

between grid points.

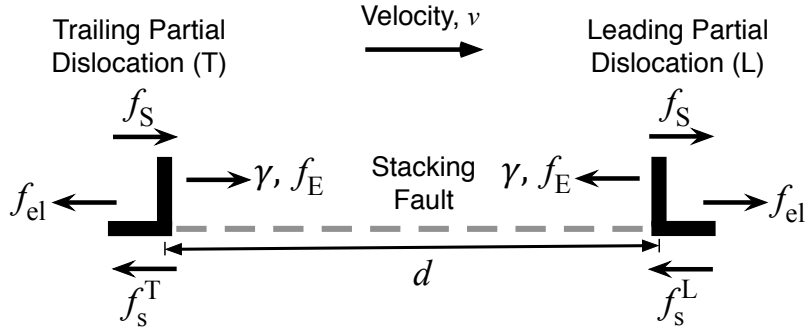

Figure 2. Force balance on an extended dislocation used to determine the separation distance, d.

The separation distance, d, still needs to be determined; we employ a simple force balance to find its value (see Fig. 2). Each partial dislocation experiences the force γ exerted by the stacking fault, f_s^L or f_s^T due to the solute atmosphere, f_{el} due to elastic interaction between the partials, and so-called Schmid and Escaig forces,

$$f_S = \frac{b}{2}\left(\tau_{xy}\sin\theta + \tau_{xz}\cos\theta\right) \tag{17}$$

$$f_E = \frac{b}{2\sqrt{3}}\left(\tau_{xz}\sin\theta - \tau_{xy}\cos\theta\right), \tag{18}$$

due to the applied stresses, τ_{xy} and τ_{xz}. Note the directions of the forces in Fig. 2 for sign conventions. At steady-state, the sum of the forces on each partial must balance, giving two equations which can be combined to yield the relationship

$$f_s^T - f_s^L = 2\left(\hat{\gamma} - f_{el}\right), \tag{19}$$

where

$$\hat{\gamma} = \gamma + f_E \tag{20}$$

is the effective stacking fault energy. Defining $\hat{\gamma}$ in this way allows us to assess stacking fault energy effects and applied (Escaig) stress effects simultaneously. Since f_s^L, f_s^T, and f_{el} are all functions of d, the steady state separation distance can be determined by finding the root of Eq. (19), for which we employ the secant method.

By comparing our solution with the analytical result of Fuentes-Samaniego et al. [8] (see Appendix B), we found that accurate and convergent solutions were obtained using a 1000×1000 grid (or finer) of uniformly spaced points in the transformed domain, with the scaling parameter set at $\alpha = 2b$. This resulted in the smallest grid spacing in the physical domain at the dislocation core being about $0.00628b$, and the height and width (when $d = 0$) of the physical domain being about $318b$.

4. Results

To fully examine the non-dimensional force-velocity ($\overline{F}$-q) curve, we need to determine all of the dependencies in Eq. (14). We can limit the range of parameters by noting that $\frac{\hat{\gamma}}{\mu b} \approx 0.01 - 0.0001$ [22], and recognizing that the the core radius, a, in the non-singular theory roughly represents the size of the region where linear elasticity is invalid, leading to the range $\frac{a}{b} \approx 1 - 4$ [23]. The S parameter is inversely proportional to the temperature squared, so it can take a wide range of values; we restrict ourselves to the range 4–200, which corresponds to, for example, temperature ranges of about 250–1600 K and 140–950 K for the nickel-hydrogen and aluminum-magnesium systems, respectively.

We have numerically studied the effects of all six non-dimensional groups in Eq. (14); due to space constraints, only the most significant results are presented below.

4.1. *Perfect dislocations*

4.1.1. Edge dislocation

First we will consider a pure edge dislocation, i.e. $b_e = b$. We begin by visualizing the effects of dislocation motion on the concentration field. Fig. 3 shows the concentration fields surrounding a dislocation moving at velocities of (top) $q = 0$ and (bottom) $q = 1$ with concentrations of (left) $\chi_0 = 0.001$ and (right) $\chi_0 = 0.1$. We see that dislocation motion causes the concentration field to tilt along the x-axis, which gives rise to the drag force.

Before delving too deeply into the characteristics of force-velocity curves, we wish to briefly discuss the core treatment. While it may be argued that the non-singular theory provides a physically reasonable solution around the dislocation core, we must observe that it is derived using linear elasticity theory which is known to break down in the core region. Hence, in all likelihood the true behavior at the dislocation core is not being captured. Nonetheless, the non-singular theory provides a self-consistent model of the dislocation core, and guarantees numerical convergence as the mesh size becomes much smaller than the core radius. On the other hand, past results derived using the singular theory were calculated by simply neglecting the contribution from the core region on the drag force, either formally with a cut-off radius (as in Eq. (B1)) or by ignoring the grid point at the core. All results for perfect dislocations presented in the body of the paper will be with a non-singular core radius of $a = 2b$. The effects of changing a are discussed in Appendix C.

First we consider the concentration dependence of the drag force for a perfect edge dislocation, $\overline{F}_e$, as a function of q. Fig. 4 presents the results with background concentrations of $\chi_0 = 0.001$, 0.01, 0.1, and 0.25 at S values of (a) 4 and (b) 200. We see very clearly that the concentration dependence is strongly affected by S, with a stronger sensitivity as S increases. In the dilute limit, the normalized force-velocity curve is independent of χ_0, meaning the actual drag force F_e increases linearly with χ_0 (since $\overline{F}_e$ is normalized by χ_0). Here we see that at lower velocities, the normalized curve slowly shifts down as χ_0 is increased beyond the dilute limit, signifying that the drag force increases less than linearly, as observed by [7]. Furthermore, we see that the definition of the dilute limit is affected by S; when $S = 4$, both $\chi_0 = 0.001$ and 0.01 can be considered dilute (same $\overline{F}$-q curve), whereas when $S = 200$ this is clearly not the case. At high velocities, the curve is completely independent of the concentration and scales as $1/q$. Finally we note that increasing χ_0 beyond the dilute limit causes the critical velocity to increase.

The effects of the parameter S are shown in Fig. 5. We see that S has a strong effect on the entire force-velocity curve. Increasing S pushes the force-velocity curve upward. It also affects the onset of the $1/q$ tail, as shown by the straight lines. The critical velocity is fairly insensitive to S at the low concentration, but increases with S at higher concentrations.

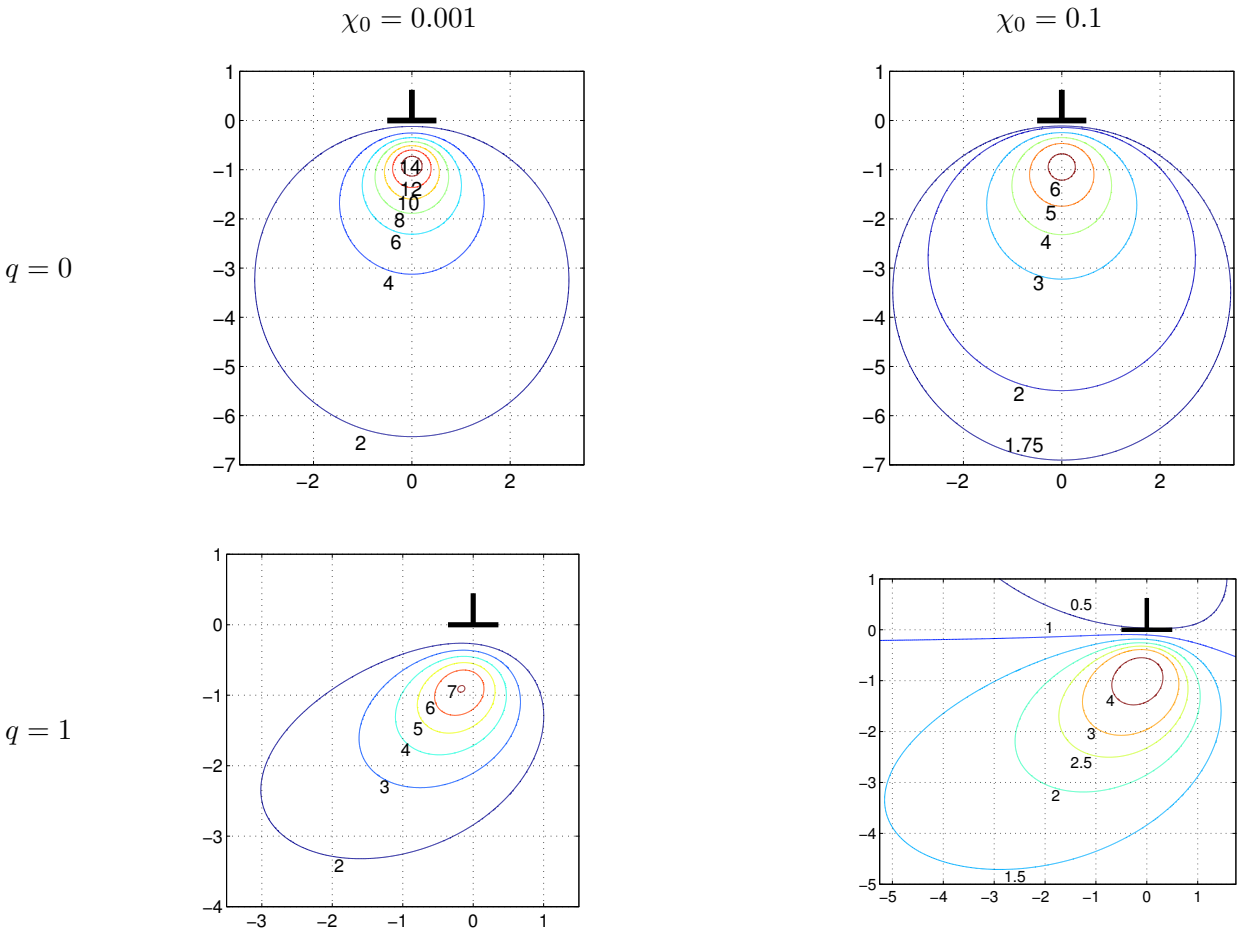

Figure 3. Contour lines of solute concentration enhancement, χ/χ_0, around an edge dislocation with $\chi_0 = 0.001$ (left) and 0.1 (right), non-dimensional velocities of $q = 0$ (top) and 1 (bottom), $S = 20$, and $a = 2b$. The grid spacing is in units of b.

To aid in understanding the effects of different parameters on the $\overline{F}$-q curve, we have extracted their major features and presented them in Fig. 6. In all of these plots, solid lines denote analytical curve fits which are given in Appendix C.

Fig. 6(a) presents the maximum drag force on a perfect edge dislocation as a function of concentration for each value of S, extracted from the $\overline{F}$-q curves by fitting them with cubic splines. For each dataset a small vertical line denotes the dilute limit. In the dilute range, $\overline{F}_e^{\max}$ is not affected by χ_0, as expected. Beyond this range the force drops towards zero at $\chi_0 = 1$, since there is no Cottrell drag in this limit. In the dilute limit, $\overline{F}_e^{\max}$ varies from 1 to 39 for $S = 4$–200, showing the estimates of 17 and 28 by Cottrell and Jaswon [3] and Cottrell [4], respectively, are valid over some range of atmosphere strengths.

The critical velocities for perfect edge dislocations, $q_{c,e}$, also extracted using a cubic spline fit, are presented in Fig. 6(b). In the dilute range, $q_{c,e}$ values are between 0.5 and 1.1, indicating that Cottrell's estimate, Eq. (11), leading to $q_{c,e} = 1$ in Table 1, is reasonable. Nonetheless, $q_{c,e}$ is not a constant; it increases sharply as the concentration increases, especially at large values of S.

Examining Table 1, we see that according to the existing theories, in the high velocity limit $\overline{F}_e$ is expected to scale with S, and be insensitive to χ_0. Figs. 4 and 5 clearly demonstrate insensitivity to χ_0 at high velocities. To examine the dependence on S, we have extracted from the $1/q$ high velocity fits both the onset velocity $q'_{c,e}$, above which the force varies as $1/q$, and the coefficient

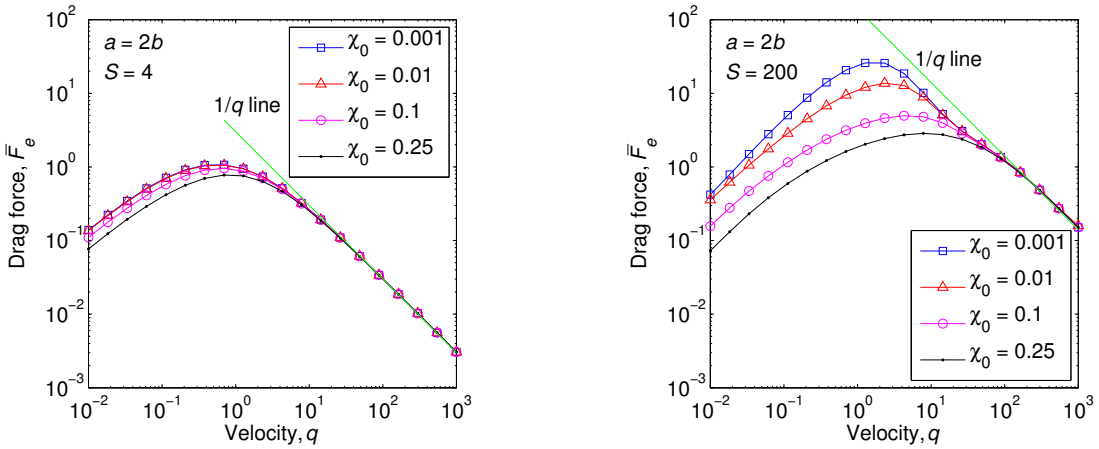

Figure 4. Force-velocity curves for a perfect edge dislocation showing the effect of the background concentration, with $\chi_0 =$ 0.001, 0.01, 0.1, and 0.25, $a = 2b$, and (a) $S = 4$ and (b) 200.

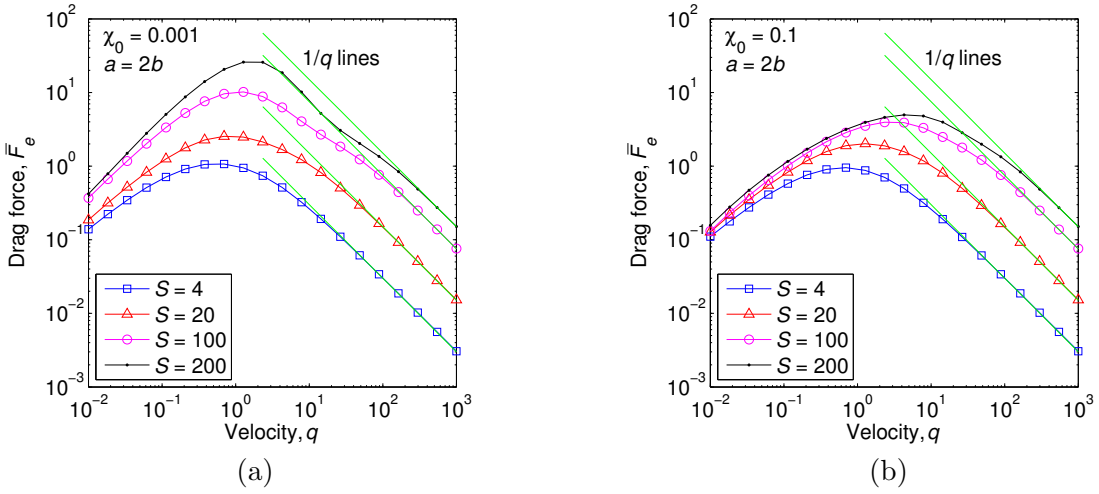

Figure 5. Force-velocity curves for a perfect edge dislocation showing the effect of S, with $S = 4$, 20, 100, and 200, $a = 2b$, and χ_0 values of (a) 0.001 and (b) 0.1.

of the fit, c'_e, such that $\overline{F}_e \approx c'_e/q$. Both of these are given in Fig. 6(c) as a function of S. The coefficient c'_e is seen to vary linearly with S, as predicted by Eq. (13) (see expression $\overline{F}_e = (\pi/4)S/q$ in Table 1). On the other hand, $q'_{c,e}$ varies sublinearly with S, in disagreement with Eq. (12) (see expression $q'_{c,e} = S/4$ in Table 1).

Finally, we have plotted the peak drag force and critical velocities in the dilute limit, $F^{\max}_{e,\mathrm{dil}}$ and $q^{\mathrm{dil}}_{c,e}$, as a function of S in Fig. 6(d). Both go to zero as S approaches zero. The critical velocity asymptotes to approximately 1.1 at large S. The peak force is seen to initially scale as $\sqrt{S}$, in agreement with Eq. (10), and then transition to an S^2 scaling.

4.1.2. Mixed and screw dislocations

To calculate the force-velocity curve for a perfect dislocation of mixed character, we simply need to rescale the results for an edge dislocation. This is because changing the character angle, θ, only affects the edge component of the Burgers vector, b_e. Using the edge results, $\overline{F}_e\left(q, \chi_0, S, \frac{a}{b}\right)$ pre-

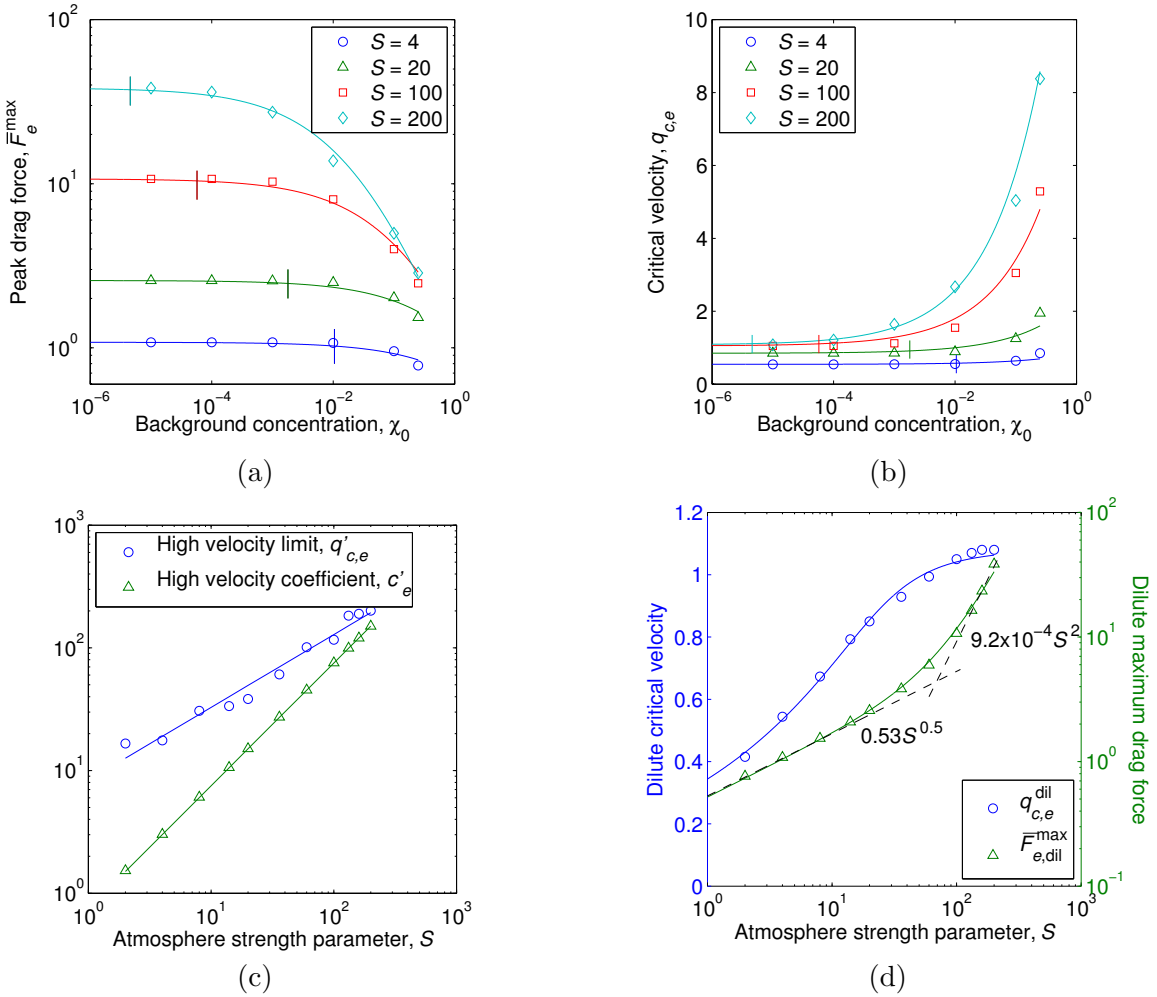

Figure 6. Features of the force-velocity curve for a perfect edge dislocation. Solid lines denote analytical curve fits given in Appendix C. Small vertical lines denote dilute limits.

sented above, the force-velocity curve for a mixed dislocation can be calculated using the following relation

$$\overline{F} = \sin|\theta|\,\overline{F}_e\left(\frac{q}{\sin|\theta|},\,\chi_0,\,S\sin^2\theta,\,\frac{a}{b}\right). \tag{21}$$

These rescalings derive simply from the fact that we have used $\hat{\beta}$ instead of β to construct our non-dimensional groups, and hence need to replace b with b_e in these groups. The drag force depends on $|\theta|$ rather than θ because the drag force direction is independent of the sign of the Burgers vector (as long as the dislocation moves in the same direction). Note that the resulting drag force on a screw dislocation is zero, since a perfect screw dislocation has no hydrostatic stress field.

4.2. *Extended dislocations*

For extended dislocations, we wish to choose the core radius so that the results can be readily compared with the perfect dislocation results, which used a core radius of $2b$. The Burgers vector

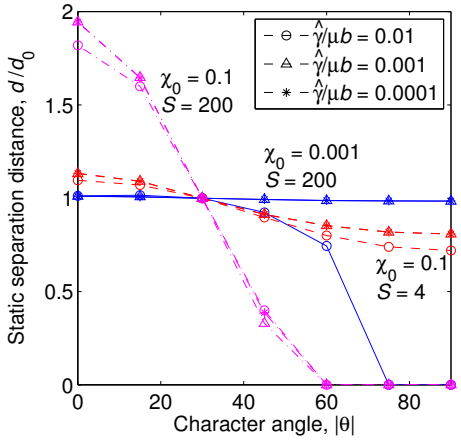

Figure 7. Separation distance, d, of a stationary extended dislocation normalized by the separation distance without solutes, d_0, as a function of character angle.

of each partial dislocation has a magnitude of $b/\sqrt{3}$ [2] , so scaling the core radius accordingly leads to $a = 2b/\sqrt{3}$ for each of the partial dislocations, which was used in all extended dislocation calculations.

Before examining how extended dislocations behave dynamically, we will assess the effects of a Cottrell atmosphere on the separation distance of a static extended dislocation. Fig. 7 shows d normalized by the solute-free separation distance, d_0, as a function of character angle $|\theta|$ for various cases. For character angles in the range $-30° < \theta < 30°$ (i.e. near screw), the separation distance is increased, and beyond this range it is reduced. These trends are due to the distribution of the atmosphere (see Fig. 8). At $\theta = \pm 30°$, one of the partials is pure screw, so that the other partial behaves as an isolated edge dislocation with a symmetric atmosphere which exerts no forces on the partial dislocations. A reduction in partial separation for edge dislocations was also observed in [20] and [24] in nickel with hydrogen atmospheres (forming "nano-hydrides"). As the concentration χ_0 and S are increased, the separation distance is modified more by the atmosphere. The separation distance of a screw dislocation is shown to nearly double in the most extreme case shown. Dislocations near edge are shown to have their separation distance go to zero; this is because in the non-singular theory there is a peak repulsive elastic force that can exist between the partials.

Fig. 8 shows the concentration fields around an (left) extended screw and an (right) extended edge dislocation with $\frac{\hat{\gamma}}{\mu b} = 0.01$, $S = 20$, $\chi_0 = 0.001$, and velocities of (top) $q = 0$ and (bottom) $q = 1$. Since a screw dislocation has no net edge component in its Burgers vector, the two partials have oppositely-signed edge components. This results in one partial having an atmosphere below the x-z plane, and the other having an atmosphere above it (anti-symmetric). Thus, while in the extended edge case the pressure fields reinforce one another, in the extended screw they act to cancel each other.

In order to fully assess the behavior of mixed extended dislocations in motion, we need to consider the character angle range $-90° < \theta \leq 90°$. When $\theta > 0°$, the trailing partial has a larger edge component than the leading partial, causing it to have a more substantial atmosphere, and to widen the stacking fault area when the dislocation is in motion. When $\theta < 0°$, the opposite is true; we will demonstrate these effects.

Fig. 9(a) presents force-velocity curves over the full range of character angles with $\chi_0 = 0.001$,

[2] It has been shown that when partial dislocations are so close that their core structures overlap, it is possible to have partial Burgers vectors that are smaller than $b/\sqrt{3}$ [19]. Here we neglect this effect, and point out that in such a case the dislocation is likely well approximated as perfect for the purposes of solute drag calculation.

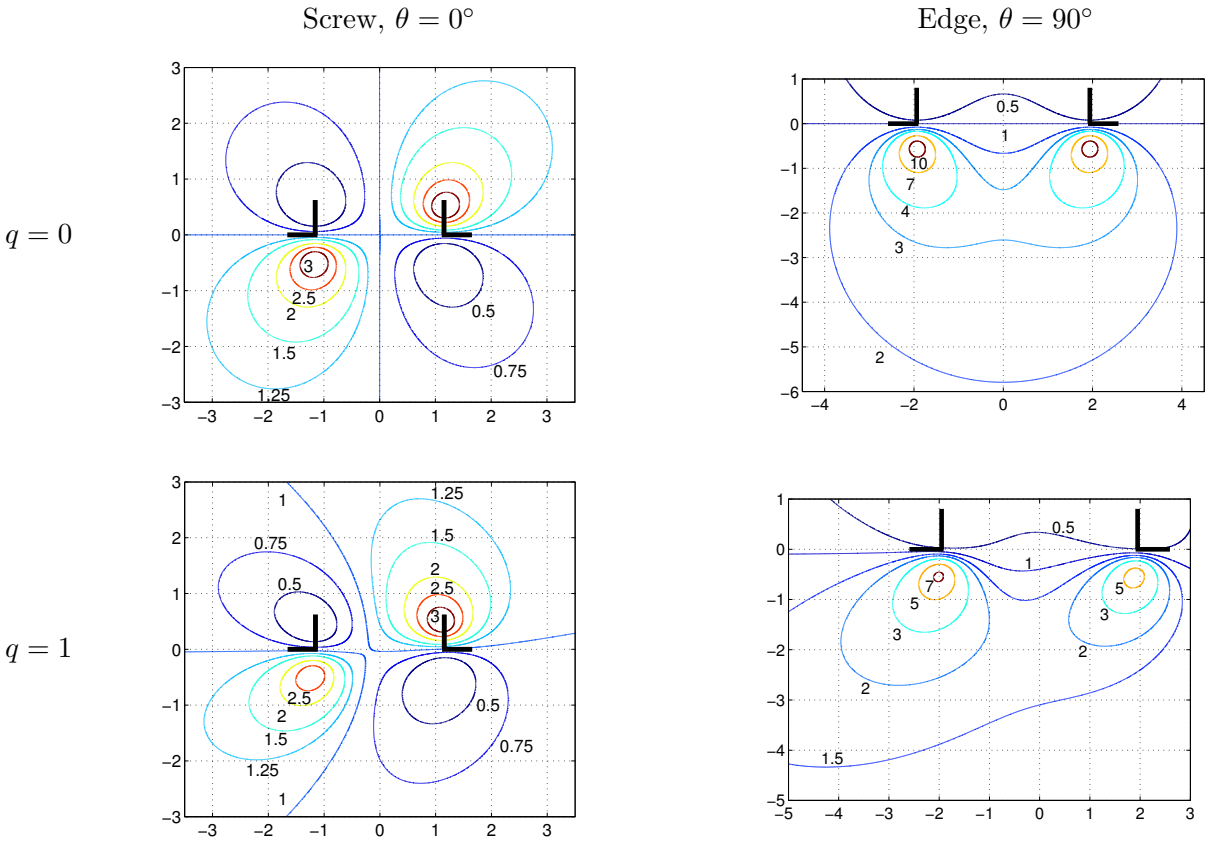

Figure 8. Contour lines of solute concentration enhancement, χ/χ_0, of extended screw (left) and edge (right) dislocations with $\chi_0 = 0.001$, $\hat{\gamma}/\mu b = 0.01$, $S = 20$, $a = 2b/\sqrt{3}$, and non-dimensional velocities of $q = 0$ (top) and 1 (bottom). The grid spacing is in units of b.

$S = 200$, and $\hat{\gamma}/\mu b = 0.001$. It shows that in the character angle range $-30° < \theta < 30°$ (near screw), the force-velocity curve is sensitive to the character of the dislocation. In contrast, the curves with $\theta = \pm 60°$ and $90°$ (near edge) are nearly identical. We also observe that the sign of the character angle does not seem to affect the $\overline{F}$-q curve, meaning the drag force can be considered a function of $|\theta|$ (even though the separation distance does depend on the sign of θ). Also shown as a black dash-dotted line is the result for a perfect edge dislocation. At low velocities the drag force on the perfect edge dislocation is larger than that on the extended dislocation, but at high velocities the reverse is true.

The character angle dependence of the separation distance as a function of velocity is shown in Fig. 9(b). The separation distance in the high velocity limit equals the solute-free separation distance, since the atmosphere is weak in this limit. For this set of parameters, the low velocity separation distance is very nearly the solute-free value as well. At intermediate velocities, where drag forces are largest, the separation distance can change significantly. In the range $-90° < \theta < 0°$ the separation distance is reduced, and vice versa for positive angles. Also shown in Fig. 9(b) are results for $\theta = -30°$ with $\chi_0 = 0.1$ and $\theta = 30°$ with $\hat{\gamma}/\mu b = 0.0001$. We see that in the former case, the separation distance drops tremendously in the intermediate velocity range, with full collapse to a perfect dislocation in some cases, and in the latter case the separation distance actually goes to infinity; we will further discuss these "instabilities" in Section 5.

To further examine the character angle dependence of the $\overline{F}$-q curve, in Fig. 10 we show how (a) the peak force and (b) the critical velocity vary with $|\theta|$ for $S = 100$, $\chi_0 = 0.001$, and SFEs of $\hat{\gamma}/\mu b = 0.01$, 0.001, and 0.0001. Also shown as a dashed line are the results for a perfect dislocation

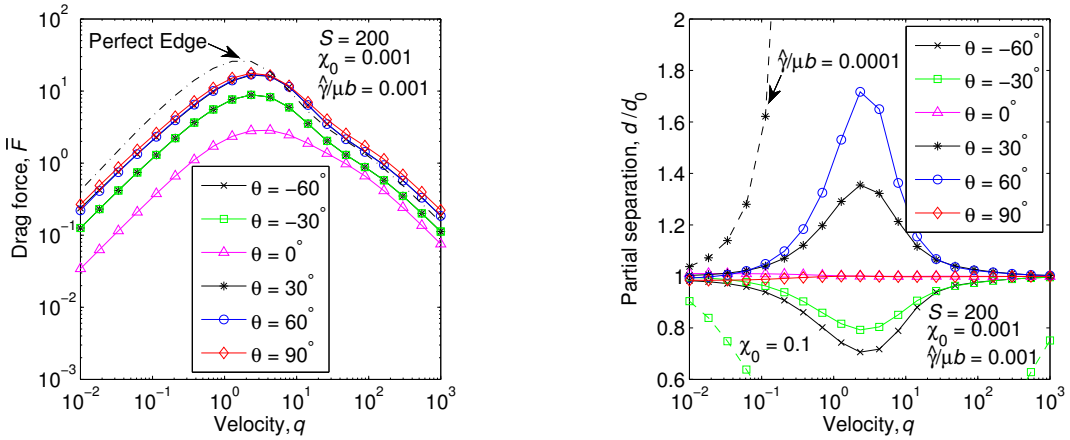

Figure 9. Character angle dependence of (a) force-velocity curves and (b) partial separation distance with $\chi_0 = 0.001$, $S = 200$, and $\hat{\gamma}/\mu b = 0.001$. Also shown in (b) are results for $\theta = -30°$ with $\chi_0 = 0.1$ and $\theta = 30°$ with $\hat{\gamma}/\mu b = 0.0001$.

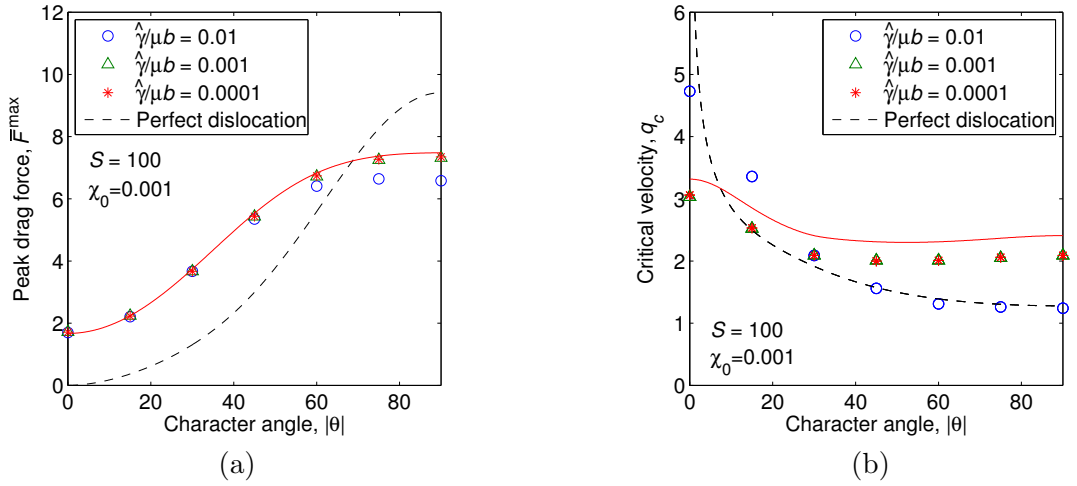

Figure 10. Effect of the character angle on (a) the peak drag force and (b) the critical velocity of an extended dislocation with $S = 100$, $\chi_0 = 0.001$, and $\hat{\gamma}/\mu b = 0.01$, 0.001, and 0.0001. Dashed lines show the results for a perfect dislocation obtained from curve fits. Solid lines are curves fits for the extended dislocation data (see Appendix C).

using the curve fits in Appendix C. Solid lines are curve fits to the extended dislocation data by approximating the extended dislocation as a superposition of two independent perfect dislocations. We can see that this approximation works well, except at the highest SFE. Whereas the drag force goes to zero for a perfect screw dislocation, the peak drag force on an extended screw is nonzero and, with this set of parameters, about a factor of 4 smaller than that for an extended edge. The ratio of the edge to screw peak drag force is found to be a function of both S and χ_0. It is important to note that other researchers have observed using atomistics that solute interactions with the dislocation core can lead to drag forces for edge and screw dislocations that are of the same order of magnitude [25]. We see the SFE has little or no effect on the drag force. At smaller SFEs, the critical velocity q_c is essentially independent of $|\theta|$, and at the largest SFE the data follows the perfect dislocation line reasonably well.

5. Discussion

5.1. *Analytical form for $\overline{F}$-q curve*

It is desirable to develop a simple analytical form that captures the major features of the force-velocity curve. For instance, in the dislocation dynamics modeling approach, a so-called mobility law is used to determine the velocity of a dislocation as a function of its local driving force. Given a function that dictates the Cottrell drag as a function of velocity, a mobility law could be defined that includes these effects, thereby providing a model for solid solution effects on dislocations. This mobility law could be used to simulate the effects of alloying or the introduction of contaminants such as hydrogen on the stress-strain curve.

Using the curve fits in Appendix C for the major features of the $\overline{F}$-q curve, we have found a simple analytical form for the entire curve. We seek a functional form that behaves as c'/q for large q, reaches the maximum value $\overline{F}^{\max}$ at q_c, and provides a good overall fit to the data. We have found that the following simple function meets all of these criteria:

$$\overline{F}(q) = \frac{c'q}{q^2 + \left(c'/\overline{F}^{\max} - 2q_c\right) q + q_c^2}. \tag{22}$$

where $\overline{F}^{\max}$, c', and q_c as functions of S, χ_0 and θ are given in Appendix C. Eq. (22) provides a simple analytical form that can be used in dislocation dynamics simulations involving solute drag.

5.2. *Instabilities of extended dislocations*

We have found that a solute atmosphere can destabilize an extended dislocation in two ways: 1) collapsing it into a perfect dislocation or 2) spreading it into an unbounded stacking fault. Both instabilities occur at low to intermediate velocities where an atmosphere is present and can exert considerable forces on the partials. Higher concentrations and larger values of S increase the tendency for these instabilities to occur, since the forces applied by the solutes are stronger.

We have seen that a dislocation can collapse both while stationary and while traveling at an intermediate velocity. At velocities away from the collapse velocity, the dislocation generally splits back into partials. Obviously collapsing instabilities are promoted by a high stacking fault energy.

Byun [26] has shown that spreading instabilities can occur in the absence of solute drag forces if the proper stress state is applied, independent of the dislocation velocity. In contrast, the spreading instabilities shown here are dynamic in nature – when the trailing partial has a much more substantial atmosphere than the leading partial and the dislocation is moving at a moderate velocity, the drag force on the trailing partial may be significant enough to rip it away from the leading partial. This instability occurs in the character angle range $0° < \theta < 90°$ since the trailing partial has a larger atmosphere in this range. The simplest case is $\theta = 30°$ where the leading partial has no atmosphere so that $f_s^{\mathrm{L}} = 0$; the dislocation destabilizes when the drag force pulling the trailing partial away exceeds the effective SFE holding them together, i.e. $f_s^{\mathrm{T}} > \hat{\gamma}$. Low SFEs allow for this instability to occur.

In general we see that a Cottrell atmosphere can significantly alter the separation distance between partial dislocations, both statically and dynamically. It is important to keep in mind that the effects shown here are not due to modification of the SFE. Rather, they are simply due to the drag forces exerted by the solutes on the partial dislocations. The question of how the presence of solutes modifies the SFE is an important one which many researchers have focused on, but we must keep in mind that multiple features of a solid solution can alter the separation distance between partial dislocations. Thus, the results of electron microscopy studies of extended dislocations in metals containing solutes must be interpreted with care. A change in stacking fault width does not

necessarily mean a change of SFE.

5.3. *Implications for plastic deformation*

A number of the effects observed in force-velocity curves are expected to have strong impacts on the plastic deformation behavior of metals. The first major effect expected is due to drag anisotropy. For perfect dislocations in isotropic elasticity and neglecting modulus mismatch effects (as in the results presented here), screw dislocations experience no Cottrell drag. With extended dislocations, we find that screw dislocations experience drag forces about a factor of 3 to 10 (for the parameter ranges considered) lower than edge dislocations. In materials and at solute concentrations and temperatures where Cottrell drag forces are significant in comparison to other drag forces in the material, e.g. phonon drag, this drag anisotropy is expected to have a strong impact on the dislocation structures that result from plastic deformation. Since screw dislocations are much more mobile, they will move at much higher velocities than edge dislocations. This type of behavior generally results in dislocation structures that are dominated by the less mobile dislocation type, in this case edges. An analogy for this type of behavior is plastic deformation in body-centered cubic (BCC) metals at low temperatures. Screw dislocations in BCC metals experience much larger lattice resistance than edge dislocations, resulting in dislocation structures that are dominated by screws [27]. Some experimental observations of the effects of solutes are consistent with edge dislocations being more prevalent. For instance, the introduction of hydrogen [28] and nitrogen [29] solutes in FCC stainless steel has been shown to increase the planarity of slip. Since only screw dislocations can cross-slip, one mechanism for increasing slip planarity is to reduce the number of screw dislocations.

Since Cottrell drag is sensitive to temperature, we expect the plastic deformation of solid solutions to be sensitive to temperature as well. The temperature appears in two non-dimensional groups: the atmosphere strength parameter S is inversely proportional to T^2 and the non-dimensional velocity q is inversely proportional to T and proportional to D (which depends exponentially on T). The first temperature effect then is to change the drag force; since the whole $\overline{F}$-q curve is shifted upward as S is increased, we expect larger drag forces at lower temperatures. We note that both of the instabilities observed in extended dislocations occur more readily at higher values of S (again because the drag forces are increased), and therefore are more likely to occur at low temperatures. The second effect is to simply rescale the abscissa of the $F(v)$ curve. At higher temperatures, solutes are more mobile and the force-velocity curve is spread out to higher physical velocities. As a consequence of this effect, Cottrell drag may not be relevant at low temperatures where solutes move much more slowly than dislocations. This fact can limit the values of S that are relevant to a material system, i.e. "large" values may not be attainable. One example where large values of S are relevant is the nickel-hydrogen system; using the parameters for this system at room temperature ($\mu = 76\,\mathrm{GPa}$, $\nu = 0.385$, $b = 2.49\,\text{Å}$, $\Delta V = 2.74\,\text{Å}^3$, $D = 1.2 \times 10^{-13}\,\mathrm{m^2/s}$ [30]), we find $S \approx 144$, and assuming a dislocation density of $\rho \approx 10^{10}\,\mathrm{m^{-2}}$ and a loading strain rate of $\dot{\epsilon} \approx 10^{-5}\,\mathrm{s^{-1}}$, the Orowan relation gives a non-dimensional velocity of $q = \dot{\epsilon}\hat{\beta}/(4Dk_\mathrm{B}Tb\rho) \approx 0.26$. Based on our results, this is well below the critical velocity and Cottrell drag is expected at room temperature.

The effects of solutes on the stability of extended dislocations is likely to impact plastic deformation as well. In particular, the spreading instability is likely to be highly consequential. If an atmosphere is able to cause a spreading instability, the result will be a very large stacking fault running across the metal. Obviously the instability will not occur in an unbounded manner; interactions with other dislocations and grain boundaries or free surfaces will eventually terminate the spreading. Stacking faults much larger than those observed between partials in pure metals should be observed, however. Direct experimental verification of this phenomena would be very challenging because it is a dynamic effect—to directly observe it will require observing a moving dislocation in a metal with solutes. Nonetheless, the stacking fault probability, the fraction of {111} planes

containing stacking faults, has been shown to increase in the FCC metal copper (which has a relatively low SFE) when it is deformed in the presence of hydrogen [31]. Futhermore, the introduction of hydrogen [32] and nitrogen [29] in stainless steel, which also has a very low SFE, is known to cause the formation of deformation twins, and ϵ martensite as well in the case of hydrogen. Both of these defects can form when layers of stacking faults form on top of each other [33–36]. This effect is also known to occur most frequently at low temperatures and high concentrations, where spreading instabilities are most common (as noted above).

5.4. *Example for the stainless steel-hydrogen system*

To give an example for how to use our results in a real material system, we now examine the case of stainless steel with hydrogen in more detail. We use the following parameters to describe a low stacking fault energy austenitic stainless steel containing interstitial hydrogen: $\mu = 65.6\,\text{GPa}$, $\nu = 0.28$, $b = 2.51\,\text{Å}$, $\gamma = 10\,\text{mJ/m}^2$ [26], and $\Delta V = 2.24\,\text{Å}^3$ [37], which results in $\hat{\beta} = 0.435\ \text{eV}\cdot\text{Å}$ and $\gamma/\mu b = 6.1\times10^{-4}$. Hydrogen occupies the octahedral interstitial sites in this material [38], so that $z = 1$ and $c_{\max} = 1/\Omega$. Note that these sites lead to purely dilatational misfit. Using gaseous hydrogen charging, concentrations of $\chi_0 = 0.01$ are commonly obtained. To assess the potential for a spreading instability, drag calculations can be performed with $\theta = 30°$ (spreading occurs most readily with this character angle). Since the leading partial has no atmosphere, we can use the $\overline{F}$-q curve for a perfect dislocation with an edge Burgers vector component of $b_{\text{e}}^{\text{T}} = b_{\text{p}}\sin(60°) = b/2$ for the trailing partial, and predict a spreading instability when $F > \gamma$. As we increase S by decreasing the temperature the drag force increases, and we can determine the S value (temperature) where $F^{\max} = \gamma$; this provides an estimate for the temperature boundary below which we expect spreading instabilities to occur—what can be referred to as the twinning temperature. Using the curve fits in Appendix C.3, we can express the the peak drag force on the trailing partial as

$$F^{\max} = \chi_0\, c_{\max}\,\hat{\beta}\left(\frac{b_{\text{e}}^{\text{T}}}{b}\right)\left\{c_F\left(S_{\text{eff}}(a)\left(\frac{b_{\text{e}}^{\text{T}}}{b}\right)^2\right)\sqrt{\chi_0} + \left[\overline{F}_{e,\text{dil}}^{\max}\left(S_{\text{eff}}(a)\left(\frac{b_{\text{e}}^{\text{T}}}{b}\right)^2\right)\right]^{-1/2}\right\}^{-2} \tag{23}$$

where $c_F(\cdot)$, $\overline{F}_{e,\text{dil}}^{\max}(\cdot)$, and $S_{\text{eff}}(a)$ are defined in the appendix. With the above parameters (and using $a = 2b/\sqrt{3}$), we find that $F^{\max} = \gamma$ when $S \approx 43$, which corresponds to a twinning temperature of $T \approx 300\,\text{K}$. Of course this analysis assumes that dislocations reach the critical velocity during deformation. Again taking $\rho \approx 10^{10}\,\text{m}^{-2}$ and $\dot{\epsilon} \approx 10^{-5}\,\text{s}^{-1}$, and using a diffusivity of $D = (6\times10^{-7}\,\text{m}^2/\text{s})\exp\left[-0.56\,\text{eV}/(k_{\text{B}}\,300\,\text{K})\right] = 2.4\times10^{-16}\,\text{m}^2/\text{s}$ [39], we compute with the Orowan relation $q = \dot{\epsilon}\hat{\beta}/(4Dk_{\text{B}}Tb\rho) \approx 7$. Hence, it is plausible that peak drag is operative. Deformation twinning has been observed at room temperature and below [32]. However, to our knowledge deformed microstructures of hydrogen-effected stainless steel have not been examined at elevated temperatures, so we cannot precisely evaluate the accuracy of this twinning temperature. Also, keep in mind that hydrogen is thought to reduce the SFE of stainless steels [40], which would lead to an increase in this boundary. Finally, using the curve fits we have computed the dimensional $F(v)$ curve for a $\theta = 30°$ dislocation at $T = 320$ K—just above the twinning temperature—which corresponds to $S \approx 40$, and plotted it in Fig. 11 along with the numerically computed curve. This provides the reader an order of magnitude for the forces and velocities involved, and demonstrates the accuracy of the curve fits.

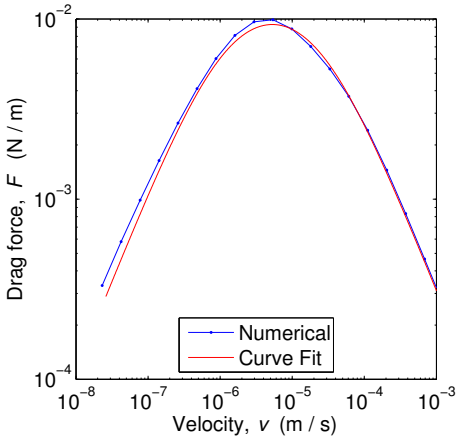

Figure 11. Dimensional force-velocity curve for a $\theta = 30°$ dislocation in stainless steel with hydrogen solutes at a concentration of $\chi_0 = 0.01$ and at $T = 320$ K. Curves are shown using the numerically computed curve (with $S = 40$) and the curve produced with the curve fits in Appendix C. See text for material parameters used.

6. Conclusions

Cottrell drag due the presence of a solute atmosphere has been thoroughly assessed for both perfect and extended dislocations. All dependencies of the resulting force-velocity curve and its major features have been found in terms of non-dimensional groups. Analytical fits have been given for nearly all of these features, and for the force-velocity curve itself. This provides a complete assessment of Cottrell drag in the context of the given model (isotropic linear elastic material, dilatational solute misfit, no modulus mismatch, steady-state concentration field), and paves the way for future studies that can incorporate additional features such as transience, anisotropy, modulus mismatch, and non-dilatational misfits.

The primary differences between the results for extended and perfect dislocations are that extended screw dislocations experience non-zero drag forces, and extended dislocations can experience spreading and collapsing instabilities. The spreading instability is expected to lead to an increase in the total stacking fault area and possibly the introduction of deformation twins and phase transformations. The separation distance of stationary extended dislocations is also modified by a Cottrell atmosphere (without changing the SFE); thus, caution should be exercised when attempting to determine the stacking fault energy dependence on solute concentration.

The present results can be utilized in several ways. First, order of magnitude assessments can be performed by comparing basic features of the $\overline{F}$-q curve with experimental parameters. For instance, the critical dislocation velocity can be compared with the applied strain rate using the Orowan relation. In this way, the operative modes of solute drag can be determined, and rough estimates can be made of their effects. Secondly, our results can be used to provide input for dislocation dynamics simulations. Using the given analytical fits, a mobility law for a metal containing solutes can be established. Combining our results with a model for frictional drag, and an estimate of the effect of solutes on dislocation-dislocation interactions, would give a fairly complete picture for dislocation dynamics simulations of solid-solution systems.

Acknowledgements

The authors thank C. W. San Marchi, D. M. Barnett, and W. D. Nix for helpful comments and insight.

Funding

This work was supported by Sandia National Laboratories (R.B.S.) and by the U.S. Department of Energy, Office of Basic Energy Sciences, Division of Materials Sciences and Engineering under Award No. DE-SC0010412 (W.C.). Sandia National Laboratories is a multi-program laboratory managed and operated by Sandia Corporation, a wholly owned subsidiary of Lockheed Martin Corporation, for the U.S. Department of Energy's National Nuclear Security Administration under contract DE-AC04-94AL85000.

Appendix A. Calculation of drag force on a non-singular dislocation

A.1. *Pressure field of the dislocation*

We consider an infinitely long dislocation pointing in the z-direction with its center at the position (x_c, y_c). In the non-singular theory of dislocations [12], the Burgers vector is distributed isotropically according to the spreading function $\tilde{w}(R, a)$, where $R = \sqrt{(x - x_c)^2 + (y - y_c)^2 + z^2}$, the distance from the dislocation core, and a is the core spreading radius. [12] show that the spreading function can be approximated by

$$\tilde{w}(R, a) = (1 - m)w(R, a_1) + mw(R, a_2) \tag{A1}$$

where

$$w(R, a_i) = \frac{15}{8\pi}\left(\frac{1}{a_i^3(R^2/a_i^2 + 1)^{7/2}}\right), \tag{A2}$$

$a_1 = 0.9038a$, $a_2 = 0.5451a$, and $m = 0.6576$. We note that this is only an approximate fit, accurate to within 0.2%, and an exact analytical form could not be found. We also note that in [12] stress expressions were given with respect to w, so that stress expressions with respect to $\tilde{w}$ can be approximated in the same manner as Eq. (A1). Hence, the pressure field for a dislocation used in this work is

$$p_{\mathrm{d}}(x, y, a) = (1 - m)\hat{p}_{\mathrm{d}}(x, y, a_1) + m\hat{p}_{\mathrm{d}}(x, y, a_2) \tag{A3}$$

where

$$\hat{p}_{\mathrm{d}}(x, y, a_i) = \frac{\mu b_{\mathrm{e}}}{3\pi}\frac{(1 + \nu)}{(1 - \nu)}\frac{(y - y_c)\left[(x - x_c)^2 + (y - y_c)^2 + 2a_i^2\right]}{\left[(x - x_c)^2 + (y - y_c)^2 + a_i^2\right]^2}. \tag{A4}$$

A.2. *Force on the dislocation from solutes*

The shear stress field at point (x, y) of a line of unit dilation ($\Delta V = 1$) parallel to the z-axis and passing through point (x', y') is [18]

$$\sigma_{xy}^{\mathrm{dila}}(x, y; x', y') = -\frac{\mu}{3\pi}\frac{1 + \nu}{1 - \nu}\frac{2(x - x')(y - y')}{((x - x')^2 + (y - y')^2)^2} \tag{A5}$$

The Peach-Koehler force from this line of unit dilatation on a non-singular edge dislocation centered at (x_c, y_c) is

$$F^{\text{dila}}(x_c, y_c; x', y') = \int_{-\infty}^{\infty}\int_{-\infty}^{\infty}\int_{-\infty}^{\infty} b_e\, \tilde{w}(x - x_c, y - y_c, z, a)\, \sigma_{xy}^{\text{dila}}(x, y; x', y')\, dxdydz. \tag{A6}$$

The interpretation of Eq. (A6) is that the total force on the dislocation is given by the sum of all the forces on each infinitesimal piece of the Burgers vector distributed over three dimensional space. If we instead were to consider a traditional, Volterra dislocation, the Burgers vector distribution function would be $\delta^3(x - x_c, y - y_c, z)$, where δ^3 is the three-dimensional delta function, and the force would thus simply be $b_e\sigma_{xy}^{\text{dila}}(x_c, y_c; x', y')$—the usual Peach-Koehler expression.

Using the approximation for the Burgers vector distribution function as given in Eq. (A1), the integral in Eq. (A6) can be performed analytically to give,

$$F^{\text{dila}}(x_c, y_c; x', y') = -\frac{\mu\, b_e}{3\pi}\frac{1+\nu}{1-\nu}\, 2(x' - x_c)(y' - y_c)\left[(1-m)\left(\frac{1}{r_{a_1}^4} + \frac{2a_1^2}{r_{a_1}^6}\right) + m\left(\frac{1}{r_{a_2}^4} + \frac{2a^2}{r_{a_2}^6}\right)\right] \tag{A7}$$

where

$$r_{a_i} \equiv \sqrt{(x' - x_c)^2 + (y' - y_c)^2 + a_i^2}. \tag{A8}$$

Now, given the distribution of solutes $\chi(x, y)$, the total Peach-Koehler force exerted by the solutes on the dislocation is

$$F(x_c, y_c) = \int_{-\infty}^{\infty}\int_{-\infty}^{\infty} c_{\max}\left[\chi\left(x', y'\right) - \chi_0\right]\Delta V F^{\text{dila}}(x_c, y_c; x', y')\, dx'dy' \tag{A9}$$

Eq. (A9) can be numerically integrated to determine the drag force on a dislocation due to a Cottrell atmosphere.

Appendix B. Comparison with analytical solution

Fuentes-Samaniego et al. [8] have found that the dilute limit, steady-state drag force on a gliding singular edge dislocation in the limit of low velocities ($v \ll v_c$) is

$$F = \pi\beta\chi_0 c_{\max}\left(\frac{v}{v_c}\right)\ln\left(\frac{\lambda v_c}{v}\right) \tag{B1}$$

where λ is defined by

$$\frac{1}{2}\ln(\lambda) = \ln\left(\frac{A}{r_c}\right) + \sum_{n=0}^{\infty}\frac{(A/r_c)^{2n}}{n(n!)\,(n+2)!} + \frac{1 - 2I_1(A/r_c)\,K_1(A/r_c)}{(A/r_c)^2},$$

$$A \equiv \frac{\beta}{2k_{\text{B}}T},$$

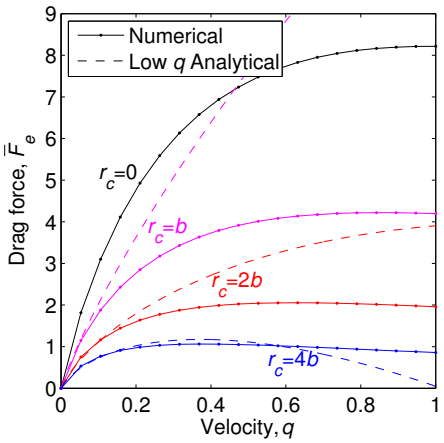

Figure B1. Force-velocity curves with $\chi_0 = 0.0001$, $S = 20$, $a = b$, and $r_c = 0$, b, $2b$, and $4b$. Solid curves are numerical results from this work. Dashed curves are the corresponding low velocity analytical results from Eq. (B1) for each of the cut-off radii (except $r_c = 0$ since the resulting force is infinite).

r_c is the cut-off radius used to avoid the singularity at the dislocation core, v_c is given by Eq. (11), and I_1 and K_1 are modified Bessel functions of the 1st and 2nd kind, respectively.

Here we will use this solution to verify our numerical implementation. To compare this solution with our results, we must enforce a cut-off radius, r_c, when calculating the drag force; otherwise, solutes within the core will contribute forces that are explicitly excluded from the analytical result. To impose this cut-off we simply set $\chi = \chi_0$ within the cut-off region during the force calculation. Fig. B1 presents force-velocity curves with linear axes over the range $q = 0$ to 1 with $\chi_0 = 0.0001$, $S = 20$, $a = b$, and $r_c = 0$, b, $2b$, and $4b$. We see that the numerical and analytical solutions match well at velocities below about $q = 0.1$, as expected. Our results also capture the effect of the cut-off radius on the force-velocity curve. Since the non-singular theory was used to calculate the numerical concentration field, whereas the classical singular theory was used in deriving the analytical solution, Fig. B1 demonstrates that the concentration field outside of the core region is not very sensitive to the core treatment.

Appendix C. Analytical fits for the $\overline{F}$-q curve

In this appendix we give analytical curve fits for the data shown in Figs. 6 and 10. Fitting parameters were determined by minimizing the L_2 norm of the error using the MATLAB function `fminsearch`.

C.1. *Effects of the core radius*

The $\overline{F}$-q curve is influenced by the core radius, a. All of the results given above correspond to a core radius of $a = 2b$ for a perfect dislocation. We have found that for a perfect dislocation, a change in the core radius can be very well approximated using the following scaling analysis. In the non-singular theory, the minimum pressure in the stress field of a stationary dislocation is proportional to the factor $(a/b)^{-1}\sqrt{S}$. If we make the assumption that the $\overline{F}$-q curve scales with this minimum pressure, then a change in a/b is equivalent to a change in S. This means we can define the effective S parameter,

$$S_{\text{eff}}(a) \equiv \left(\frac{2b}{a}\right)^2 S, \tag{C1}$$

Feature	*Eq.*
Peak Force	$\overline{F}_e^{\max}(\chi_0, S) = \left[c_F(S)\sqrt{\chi_0} + 1/\sqrt{\overline{F}_{e,\mathrm{dil}}^{\max}(S)}\right]^{-2}$ $c_F(S) = 0.0033\,S + 0.24$ $\overline{F}_{e,\mathrm{dil}}^{\max}(S) = 0.518\sqrt{S} + 6.52\times10^{-4}S^2$
Critical Velocity	$q_{c,e}(\chi_0, S) = q_{c,e}^{\mathrm{dil}}(S) + 0.075\,S\sqrt{\chi_0}$ $q_{c,e}^{\mathrm{dil}}(S) = 1.08\left[\frac{2}{\pi}\arctan\left(0.026S^{1.15}\right)\right]^{0.279}$
High Velocity Threshold	$q'_{c,e}(S) = 8.35\,S^{0.593}$
High Velocity Coefficient	$c'_e(S) = 0.752\,S$

which will capture the effect of deviation of the core radius a from $2b$ if S_{eff} is used in place of S. The validity of this approach has been confirmed against numerical results with $a = 3b$ and $4b$. Since all of the curve fits below apply to a core radius of $2b$, they can be used to determine the $\overline{F}$-q for any core radius by simply substituing $S_{\mathrm{eff}}(a)$ for S.

C.2. *Perfect dislocations*

The curve fits in the table below apply to the data presented in Fig. 6 for a perfect edge dislocation.

$\overline{F}_{e,\mathrm{dil}}^{\max}(S)$ and $q_{c,e}^{\mathrm{dil}}(S)$ are the peak force and critical velocity in the dilute limit, respectively, for the chosen value of S. The $\overline{F}_{e,\mathrm{dil}}^{\max}(S)$ expression is a generalization of the result in Hirth and Lothe [10] (see $\overline{F}_e^{\max} = \sqrt{S}$ in Table 1) that is only valid for small S.

Note that the $\overline{F}_e^{\max}$ expression does not go to zero when $\chi_0 \to 1$, so it should not be used beyond $\chi_0 = 0.25$ (the largest concentration it was fitted to).

If the $\overline{F}$-q curve for a mixed dislocation is desired, the above fits must be used in conjunction with the rescaling defined in Eq. (21).

C.3. *Extended dislocations*

We have found that the $\overline{F}$-q curve for an extended dislocation is very well approximated as the sum of two perfect dislocation $\overline{F}$-q curves—one for each partial. In this approximation, we assume that the atmospheres of the two partials do not interact, so that each partial can be treated as an isolated perfect dislocation. The only constraint is that both partials move at the same velocity q, and their drag forces are added to give the total drag force. This approximation is most valid when the partials are far apart, hence at low SFEs. When the SFE is large, an extended dislocation is better approximated as a perfect dislocation. Thus, we approximate the $\overline{F}$-q curve of an extended dislocation as follows:

$$\overline{F} = \begin{cases} \left(\frac{|b_e^{\mathrm{L}}|}{b}\right)\overline{F}_e\left(q\left(\frac{|b_e^{\mathrm{L}}|}{b}\right)^{-1},\,\chi_0,\,S_{\mathrm{eff}}(a^{\mathrm{L}})\left(\frac{|b_e^{\mathrm{L}}|}{b}\right)^2\right) \\ \qquad + \left(\frac{|b_e^{\mathrm{T}}|}{b}\right)\overline{F}_e\left(q\left(\frac{|b_e^{\mathrm{T}}|}{b}\right)^{-1},\,\chi_0,\,S_{\mathrm{eff}}(a^{\mathrm{T}})\left(\frac{|b_e^{\mathrm{T}}|}{b}\right)^2\right), & \hat{\gamma}/\mu b \lesssim 0.01 \\ \sin|\theta|\,\overline{F}_e\left(\frac{q}{\sin|\theta|},\,\chi_0,\,S_{\mathrm{eff}}(a)\sin^2\theta\right), & \hat{\gamma}/\mu b \gtrsim 0.01 \end{cases}$$

where we have made use of the rescaling for a mixed perfect dislocation discussed in Section 4.1.2, and b_e^{L} and b_e^{T} are the edge components of the leading and trailing partial Burgers vectors,

respectively. a^{L} and a^{T} are the core radii of the partial dislocations; we used $a^{\mathrm{L}} = a^{\mathrm{T}} = 2b/\sqrt{3}$ for our numerical results, however any value can be used. The absolute values in the expressions are present because the drag force direction is independent of the sign of the Burgers vector (always opposes direction of motion).

References

[1] Cottrell A. H. *Effect of Solute Atoms on the Behaviour of Dislocations*, Report of a Conference on Strength of Solids, Phys. Soc., London (1948).

[2] Cottrell A. H. and Bilby B. A. *Dislocation Theory of Yielding and Strain Ageing of Iron*, Proc. Phys. Soc. A 62, 49-62 (1949).

[3] Cottrell A. H. and Jaswon M. A. *Distribution of solute atoms round a slow dislocation*. Proc. Phys. Soc. A 199, 104-114 (1949).

[4] Cottrell, A. H. *Dislocations and Plastic Flow in Crystals*, Oxford University Press (1953).

[5] Yoshinaga H. and Morozumi S. *The solute atmosphere round a moving dislocation and its dragging stress*. Phil. Mag. 23, 1367-1385 (1971).

[6] Takeuchi S. and Argon A.S. *Glide and climb resistance to the motion of an edge dislocation due to dragging a Cottrell atmosphere*. Phil. Mag. A 40, 65-75 (1979)

[7] James W. and Barnett D.M. *A Re-examination of atmospheres and impurity drag on moving dislocations*. Proc. from Solute-Defect Interaction: Theory and Experiment, Kingston, Canada, 136-142 (1985).

[8] Fuentes-Samaniego R., Gasca-Neri R., and Hirth J.P. *Solute drag on moving edge dislocations*. Phil. Mag. A **49**, 31-43 (1984).

[9] Zhang F. and Curtin W.A. *Atomistically informed solute drag in Al-Mg*. Modelling Simul. Mater. Sci. Eng. 16 (2008).

[10] Hirth J.P. and Lothe J. *Theory of Dislocations*. Wiley, New York, NY (1982).

[11] Argon A.S. *Strengthening Mechanisms in Crystal Plasticity*. Oxford University Press (2008).

[12] Cai, W., Arsenlis, A., Weinberger, C. R., and Bulatov, V. V. *A non-singular continuum theory of dislocations*, J. Mech. Phys. Solids **54**, 561-587 (2006).

[13] Olmsted D. L., Phillips R., and Curtin W. A. *Modelling diffusion in crystals under high internal stress gradients*. Modelling Simul. Mater. Sci. Eng. 12, 781-797 (2004).

[14] Dontsova E., Rottler J., and Sinclair C. W. *Solute segregation kinetics and dislocation depinning in a binary alloy*. Phys. Rev. B, 91, 224103 (2015).

[15] Damask A. C. and Dienes G. J. *Point Defects in Metals*, Gordon and Breach, New York (1963).

[16] McLellan R. W. *Solution Thermodynamics*. In Treatise on Materials Science and Technology Vol. 5, Eds. Herman H., Academic Press, New York (1974).

[17] Fuentes-Samaniego R., Nix W. D., and Pound G. M. *Vacancy and substitutional solute distribution around an edge dislocation in equilibrium and in steady-state glide motion*. Phil. Mag. A 42, 591-600 (1980).

[18] Cai W., Sills R.B., Barnett D.M., and Nix W.D. *Modeling a distribution of point defects as misfitting inclusions in stressed solids*. J. Mech. Phys. Sol. 66, 154-171 (2014).

[19] Szelestey P., Patriarca M., and Kaski K. *Computational study of core structure and Peierls stress of dissociated dislocations in nickel*. Modelling Simul. Mater. Sci. Eng. **11**, 883-895 (2003).

[20] von Pezold J., Lymperakis L., and Neugebeauer J. *Hydrogen-enhanced local plasticity at dilute bulk H concentrations: The role of HH interactions and the formation of local hydrides*. Acta Mater. 59, 2969-2980 (2011).

[21] Moin P. *Fundamentals of Engineering Numerical Analysis*. Cambridge University Press, New York, NY (2010).

[22] Nabarro, F. R. N., Basinski, Z. S., and Holt, D. B. *The plasticity of pure single crystals*. Advances in Physics **13** 193-323 (1964).

[23] Hull, D. and Bacon, D. J., *Introduction to Dislocations*, Butterworth-Heinemann (2001).

[24] Leyson G. P. M., Grabowski B., and Neugebauer J. *Multiscale description of dislocation induced nanohydrides*. Acta Mater. 89, 50-59 (2015).

[25] Patinet S. and Proville L. *Depinning transition for a screw dislocation in a model solid solution*. Phys. Rev. B **78**, 104109 (2008).

[26] Byun T.S. *On the stress dependence of partial dislocation separation and deformation microstructure in austenitic stainless steels*. Acta Mater. 51, 3063-3071 (2003).

[27] Christian J. W. *Some Surprising Features of Plastic Deformation of Body-Centered Cubic Metals and Alloys*. Metall. Trans. A 14A, 1237-1256 (1983).

[28] Nibur K. A., Bahr D. F., and Somerday B. P. *Hydrogen effects on dislocation activity in austenitic*

stainless steel. Acta Mater. 54, 2677-2684 (2006).

[29] Müllner P., Solenthaler C., Uggowitzer P., and Speidel M.O. *On the effect of nitrogen on the dislocation structure of austenitic stainless steel*. Mat. Sci. Eng. A164, 164-169 (1993).

[30] Lee S.-M. and Lee J.-Y. *The Transport and Trapping Phenomena of Hydrogen in Nickel*. Met. Trans. A 17A 181-187 (1986).

[31] Rudee M. L. and Huggins R. A. *The Effect of Hydrogen on the Stacking Fault Probability of Copper*. Phys. Stat. Sol. 4 K101-K103 (1964).

[32] San Marchi C., Somerday B. P., and Jackson H. F. *Hydrogen-Assisted Deformation and Fracture of Austenitic Stainless Steels*. 2nd International Conference of Engineering Against Fracture, June 2011, Mykonos, Greece.

[33] Cohen J. B. and Weertman J. *A dislocation model for twinning in f.c.c. metals*. Acta Metall. 11, 996-998 (1963).

[34] Christian J. W. and Mahajan S. *Deformation Twinning*. Prog. Mat. Sci. 39, 1-157 (1995).

[35] Fujita H. and Ueda S. *Stacking Faults and F.C.C.* $(\gamma) \rightarrow$ *H.C.P.* (ϵ) *Transformation in 18/8-Type Stainless Steel*. Acta Metall. 20, 759-767 (1972).

[36] Nishiyama Z. *Martensitic Transformation*. Academic Press, New York (1978).

[37] Ulmer D. G. and Altstetter C. J. *Phase relations in the hydrogen-austenite system*. Acta Metallugica et Materialia 41, 22352241 (1993).

[38] Hoelzel M., Danilkin S. A., Ehrenberg, H., Toebbens D. M., Udovic T. J., Fuess H., and Wipf, H. *Effects of high-pressure hydrogen charging on the structure of austenitic stainless steels*. Mat. Sci. Eng. A 384 255-261 (2004).

[39] San Marchi C., Somerday B. P. , and Robinson S. L. *Permeability, solubility and diffusivity of hydrogen isotopes in stainless steels at high gas pressures*. Int. J. Hydrogen Energy 32, 100-116 (2007).

[40] Ferreira P. J., Robertson I. M., and Birnbaum H. K. *Influence of Hydrogen on the Stacking-Fault Energy of an Austenitic Stainless Steel*. Materials Science Forum, Vols. 207-209, 93-96 (1996).